Delivery of Acid Sphingomyelinase in Normal and Niemann-Pick Disease Mice Using Intercellular Adhesion Molecule-1-Targeted Polymer Nanocarriers[S]

Carmen Garnacho, Rajwinder Dhami, Eric Simone, Thomas Dziubla, John Leferovich, Edward H. Schuchman, Vladimir Muzykantov, and Silvia Muro

Department of Pharmacology (C.G., V.M., S.M.), Institute for Environmental Medicine (C.G., E.S., J.L., V.M., S.M.), Institute for Translational Medicine and Therapeutics (V.M., S.M.), School of Medicine, and Department of Bioengineering (E.S.), School of Engineering and Applied Sciences, University of Pennsylvania, Philadelphia, Pennsylvania; Department of Chemical and Materials Engineering, University of Kentucky, Lexington, Kentucky (T.D.); and Genetics and Genomic Sciences, Mount Sinai School of Medicine, New York, New York (R.D., E.H.S.)

ABSTRACT

Type B Niemann-Pick disease (NPD) is a multiorgan system disorder caused by a genetic deficiency of acid sphingomyelinase (ASM), for which lung is an important and challenging therapeutic target. In this study, we designed and evaluated new delivery vehicles for enzyme replacement therapy of type B NPD, consisting of polystyrene and poly(lactic-coglycolic) acid polymer nanocarriers targeted to intercellular adhesion molecule (ICAM)-1, an endothelial surface protein up-regulated in many pathologies, including type B NPD. Real-time vascular imaging using intravital microscopy and postmortem imaging of mouse organs showed rapid, uniform, and efficient binding of fluorescently labeled ICAM-1-targeted ASM nanocarriers (anti-ICAM/ASM nanocarriers) to endothelium after i.v. injection in mice. Fluorescence microscopy of lung alveoli actin, tissue histology, and ^{125}I-albumin blood-to-lung transport showed that anti-ICAM nanocarriers cause neither detectable lung injury, nor abnormal vascular permeability in animals. Radioisotope tracing showed rapid disappearance from the circulation and enhanced accumulation of anti-ICAM/^{125}I-ASM nanocarriers over the nontargeted naked enzyme in kidney, heart, liver, spleen, and primarily lung, both in wild-type and ASM knockout mice. These data demonstrate that ICAM-1-targeted nanocarriers may enhance enzyme replacement therapy for type B NPD and perhaps other lysosomal storage disorders.

The lysosomal storage diseases comprise more than 40 clinical conditions, primarily caused by inherited deficiencies of lysosomal hydrolases (Futerman and van Meer, 2004). Intracellular accumulation of nondegraded substrates in these disorders results in multiorgan dysfunction, high morbidity, and premature mortality (Futerman and van Meer, 2004). A viable treatment for these conditions is enzyme replacement therapy (ERT) (Desnick and Schuchman, 2002), which consists of i.v. infusion of recombinant enzymes containing sugar residues (mannose and/or mannose-6-phosphate) to target the corresponding cell receptors in different tissues (Neufeld, 1980; Du et al., 2005).

This approach is well suited for lysosomal diseases with low or no neurological involvement, which manifest by peripheral organ dysfunction (Miranda et al., 2000; Desnick and Schuchman, 2002). This is the case for type B Niemann-Pick disease (NPD), caused by a genetic deficiency of acid sphingomyelinase (ASM), which leads to aberrant accumulation of sphingomyelin and cholesterol (Schuchman and Desnick, 2000). Type B NPD is characterized by non-neurological abnormalities affecting diverse cells types and organs, including the lung (Marathe et al., 1998; Schuchman and Desnick, 2000; Dhami et al., 2001). Several cell types in lung (and other organs) are affected by NPD, yet endothelial cells are important NPD targets as they are a considerable source of ASM, produce chemokines that cause inflammatory lung disease in type B NPD (Marathe et al., 1998), and represent a route for ERT transport to other tissues.

ABBREVIATIONS: ERT, enzyme replacement therapy; NPD, Niemann-Pick disease; ASM, acid sphingomyelinase; ASMKO, acid sphingomyelinase knockout; ICAM, intercellular adhesion molecule; PECAM, platelet/endothelial cell adhesion molecule; PLGA, poly(lactic-coglycolic) acid; PBS, phosphate-buffered solution; PEG, polyethylene glycol; ID, injected dose; LR, localization ratio; TNF, tumor necrosis factor; Ctr, control.

Preclinical studies showed that ERT leads to sphingomyelin reduction and histological and biochemical improvements in heart, liver, and spleen in ASM knockout (ASMKO) mice (He et al., 1999; Miranda et al., 2000). However, this strategy was less robust for progressive lung inflammation, which may be due in part to low pulmonary delivery of ASM after i.v. infusion (He et al., 1999; Miranda et al., 2000). ERT for type B NPD may therefore benefit from strategies directed to enhance delivery to this important, yet "difficult" target organ.

A good candidate for endothelial targeting is intercellular adhesion molecule (ICAM)-1, a transmembrane anchor for leukocytes expressed by many cell types relevant to NPD and, primarily, endothelial cells (Marlin and Springer, 1987; Springer, 1994; Muro, 2007). Contrary to determinants in the endothelial cell border (PECAM-1 and VE-cadherin), or molecules that are down-regulated (angiotensin-converting enzyme and thrombomodulin) or only transiently expressed in inflammation (selectins and vascular cell adhesion molecule-1) (Muro and Muzykantov, 2005), ICAM-1 located at the endothelial lumen is highly accessible from the circulation, and it is up-regulated in inflammation (Marlin and Springer, 1987; DeGraba et al., 2000; Muro, 2007). In addition, the lung is a natural target for compounds addressed to ICAM-1, because this vasculature represents ~30% of total endothelial surface and it receives 100% cardiac output as a first-pass area after i.v. injections (Muro and Muzykantov, 2005).

Numerous studies reported efficient endothelial targeting of anti-ICAM-conjugated isotopes, contrast probes (Villanueva et al., 1998; Weiner et al., 2001), therapeutic agents (Murciano et al., 2003; Muro et al., 2003a; Muro et al., 2006b), and liposomes and polymer carriers (Bloemen et al., 1995; Sakhalkar et al., 2003; Muro et al., 2006a). ICAM-1 targeting of polymer nanocarriers may offer advantages to systemic delivery of lysosomal ERT, e.g., these carriers can be formulated as biodegradable structures to hinder immune recognition and protect the cargo from rapid degradation (Langer, 1998; Jain et al., 2000; Moghimi and Szebeni, 2003; Panyam and Labhasetwar, 2003; Dziubla et al., 2005). Such features may become relevant for ERT of chronic lysosomal conditions by alleviating unwanted reactions to recurrent treatment.

It is noteworthy that coupling recombinant ASM to anti-ICAM polymer nanocarriers (150–300 nm in diameter) leads to efficient internalization of anti-ICAM/ASM nanocarriers by cell adhesion molecule-mediated endocytosis, a unique pathway, distinct from clathrin- and caveolar-mediated endocytosis, which fail to efficiently internalize naked ASM in disease cells (Muro et al., 2003b, 2006b; Dhami and Schuchman, 2004) and carriers larger than 200 nm in diameter (Rejman et al., 2004). Anti-ICAM/ASM nanocarriers traffic to lysosomes in disease cells and recover sphingomyelin levels (Muro et al., 2006b), necessary for further development of this promising strategy. However, the potential of this ERT approach remains to be tested in pathophysiologically relevant in vivo models.

In this work, we coupled recombinant ASM to anti-ICAM model polystyrene or biodegradable poly(lactic-coglycolic) acid (PLGA) nanocarriers (180–270 nm), and we used fluorescence imaging and isotope tracing to determine their vascular targeting, organ accumulation and effects, and ASM delivery capacity in vivo. Our results indicate that ICAM-1-targeting provides safe vascular accumulation and enhanced enzyme delivery to the disease target organs (primarily the lung) in control mice and the ASMKO mouse model for NPD.

Materials and Methods

Antibodies and Reagents. Rat monoclonal antibody against mouse ICAM-1 was YN1, used in our prior studies (Murciano et al., 2003; Muro et al., 2006a). Recombinant ASM was produced in Chinese hamster ovary cells and purified as described previously (He et al., 1999). Green-fluorescent polystyrene latex spheres, either 100 nm or 1 μm in diameter, were from Polysciences (Warrington, PA). PLGA (50:50 lactic/glycolic acid ratio; molecular mass 38 kDa) polymer was obtained from Lakeshore Biomaterials (Birmingham, AL). Na^{125}I was from PerkinElmer Life and Analytical Sciences (Wellesley, MA), and Iodogen was purchased from Pierce Chemical (Rockford, IL). Unless otherwise stated, all other reagents were from Sigma-Aldrich (St. Louis, MO).

Synthesis of PLGA Polymer Nanocarriers. PLGA nanocarriers were prepared by solvent extraction, by adding 25 mg of polymer in dry acetone (10 mg/ml) dropwise to 100 ml of phosphate-buffered solution (PBS) containing 3 wt.% Pluronic F68 [polyethylene glycol (PEG)-polypropylene glycol-PEG triblock copolymer] under stirring (Muro et al., 2006a). Acetone was removed by dialysis against PBS overnight. Particles were collected by centrifugation at 25,000g for 30 min, washed twice, and stored in PBS. Final particle concentration was determined using an enzymatic assay for lactic acid, and residual surfactant was evaluated by a colorimetric PEG assay (Dziubla et al., 2005). Size of uncoated PLGA nanocarriers was ~220 nm in diameter, as determined by dynamic light scattering (Muro et al., 2006a).

Preparation of Anti-ICAM Nanocarriers. Anti-ICAM/ASM nanocarriers and control IgG/ASM nanocarriers were prepared by coating either green fluorescent polystyrene spheres (model carriers) or PLGA nanocarriers with both recombinant ASM and anti-mouse ICAM-1, or nonspecific IgG (50:50 enzyme-to-antibody mass ratio) (Muro et al., 2006b). To trace the enzyme cargo, nanocarriers were coated by a mix of antibody, unlabeled ASM, and ^{125}I-ASM (95:5 unlabeled-to-labeled enzyme molar ratio). After separation of the free antibody and enzyme counterparts by centrifugation, the amount of ^{125}I-tracer coated onto the nanocarrier surface was determined in a gamma counter. The particle diameter, determined by dynamic light scattering (Muro et al., 2006a), was ~180 nm and ~270 for anti-ICAM/ASM polystyrene and PLGA counterparts, respectively, unless specified otherwise.

Intravital and Postmortem Imaging of Anti-ICAM/ASM Nanocarriers. Anesthetized C57BL/6 mice received i.v. injections with either 180-nm or 1-μm-diameter green fluorescent anti-ICAM/ASM nanocarriers or control IgG/ASM nanocarriers. For real-time imaging, 1-μm-diameter particles were used to achieve optimal resolution and visibility to permit single particle tracking. The mesentery was exteriorized, kept under warm humidification, and imaged in a time-lapse mode using an inverted microscope (Eclipse TE2000-U; Nikon, Melville, NY), 40× or 20× objective (Nikon), and Orca-1 charge-coupled device camera (Hamamatsu Corporation, Bridgewater, NJ). Image frames were taken every 3 s from 5 to 15 min after injection, and they were analyzed using Image-Pro 3.0 software (Media Cybernetics, Silver Spring, MD).

For imaging postmortem specimens, we collected micrographs of 180-nm green fluorescent anti-ICAM/ASM nanocarriers in intact, nonsectioned kidney, heart, liver, spleen, and abdominal muscle wall. To characterize in more detail uptake and effects of nanocarriers in the target organ, we additionally used 10-μm-thick frozen sectioned tissues. Actin cytoskeleton in pulmonary alveoli was stained with Texas Red-phalloidin in sections of lung isolated 30 min after injection of nanocarriers. Lung tissue morphology was tested by

hematoxylin and eosin staining of tissue sections of lung isolated 24 h after injection of nanocarriers. Objectives (10× and 20×) and imaging system described above were used.

Radioisotope Tracing of Anti-ICAM/ASM Nanocarriers Pharmacokinetics in Mice. Anesthetized C57BL/6 or ASM knock-out (ASMKO) mice (He et al., 1999; Miranda et al., 2000; Dhami et al., 2001) received i.v. injections with ^{125}I-ASM or ^{125}I-ASM coupled to the surface of anti-ICAM or IgG nanocarriers (either polystyrene prototype or PLGA particles). Blood samples were collected from the retro-orbital plexus at 1, 15, and 30 min after injection, and organs (kidneys, heart, liver, spleen, and lung) were collected at 30 min after injection. The radioactivity and weight of the samples was determined to calculate nanocarrier-targeting parameters, including percentage injected dose (%ID), percentage injected dose per gram of organ (%ID/g), localization ratio (LR; organ-to-blood ratio of %ID/g), and specificity index (targeted-to-untargeted LR ratio in an organ) (Muro et al., 2006a).

In parallel experiments, ^{125}I-albumin was coinjected i.v. either with saline, 5 μg of TNF-α, anti-ICAM/ASM, or IgG/ASM nanocarriers. The effect of the nanocarriers on pulmonary permeability was determined 3 h after injection as albumin leakage from the bloodstream into the lung tissue, and it was expressed as the lung-to-blood ^{125}I-albumin ratio.

All animal studies were conducted in accordance with University of Pennsylvania and Mount Sinai approved protocols and the Institute of Laboratory Animal Resources (1996), as adopted and promulgated by the National Institutes of Health.

ICAM-1 Expression in Mouse Organs. Organs were collected from C57BL/6 or ASMKO mice, and then they were homogenized at 4°C in lysis buffer containing PBS, 1× phenylmethylsulfonyl fluoride, 1× protease inhibitor cocktail (Sigma-Aldrich), 0.5% SDS, and 0.5% Triton X-100. Two hundred micrograms of total protein was electrophoresed under reducing conditions in a 4 to 15% gradient polyacrylamide gel, transferred to polyvinylidene difluoride membranes, and blotted with rat anti-mouse ICAM-1 (YN1 antibody), followed by incubation with horseradish peroxidase-conjugated goat anti-rat antibody and enhanced chemiluminescence Western blotting analysis system (Amersham Biosciences, Chalfont St. Giles, UK). Densitometric quantification was performed using computer-assisted image analysis, and the results were corrected to actin levels, used as a loading control.

Statistics. Unless otherwise stated, the data were calculated as the mean ± S.E.M., where statistical significance was determined by Student's *t* test.

Results

Fluorescence Imaging of Anti-ICAM Nanocarriers Carrying Acid Sphingomyelinase Delivered in Vivo. Anti-ICAM nanocarriers carrying recombinant ASM efficiently bind endothelial cells in culture (Muro et al., 2006b). To test whether this is the case under physiological conditions, we first visually analyzed targeting of anti-ICAM/ASM nanocarriers to the endothelium in an intact vasculature. To visualize targeting in real time, model green-fluorescent anti-ICAM/ASM polystyrene particles were injected i.v. in anesthetized C57BL/6 mice, and the particles were traced by intravital microscopy in the mesentery vasculature in a time-lapse mode (Fig. 1; Supplemental Movie 1). Imaging of mesentery vessels showed that anti-ICAM/ASM carriers (Fig. 1A; Supplemental Movie 1), but not IgG/ASM carriers (Fig. 1B; Supplemental Movie 2), flowing in the bloodstream, rapidly adhered to the endothelium within 5 min after injection. Anti-ICAM/ASM nanocarriers bound to endothelium in post-capillary venules and veins (Fig. 1A) and in small arteries (e.g., 50 μm in diameter; Fig. 2A), apparently withstanding
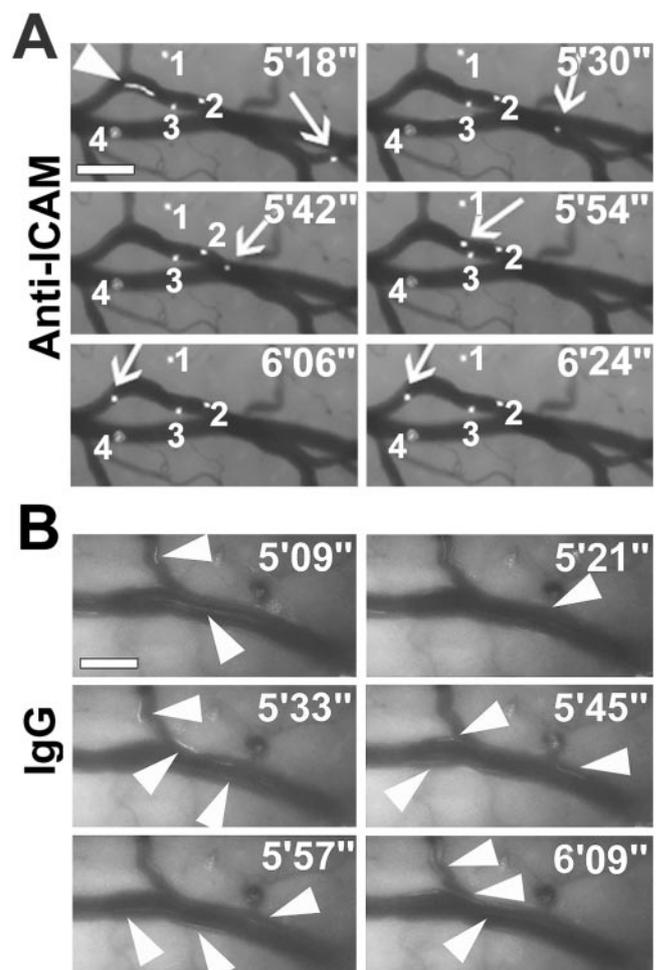

Fig. 1. Time-lapse imaging of anti-ICAM/ASM particle targeting to mouse vessels. A, time-lapse fluorescence microscopy of exteriorized mesentery vessels, taken every 3 s beginning from 5 min after i.v. injection of 1 μm of green fluorescent anti-ICAM/ASM polymer particles. Representative frames at the indicated time points are shown (see Supplemental Movie 1). Particles marked 1 to 4 were bound to the vessel from the imaging start. The arrow shows a particle slowly moving on the vessel wall, which within 1 min firmly binds and stops, as detected by lack of movement in the last two frames shown. B, time-lapse microscopy images from animals that received injections with IgG/ASM particles show lack of binding of these control particles to the vasculature (Supplemental Movie 2). The arrowheads in A and B mark tracks of particles flowing in the bloodstream. Scale bars, 10 μm.

hydrodynamic forces of shear stress levels ~20 to 50 dynes/cm^2, typical of arterial vasculature of this size.

Fluorescence microscopy images of whole (nonsectioned) organs, isolated postmortem 30 min after i.v. injection of anti-ICAM/ASM, revealed their effective uptake in all vascularized tissues examined, including heart, kidney, liver, spleen, abdominal muscle wall (Fig. 3A), mesentery (data not shown), and, most prominently, in lung (Figs. 3A and 4A). In the control IgG/ASM nanocarriers, fluorescence microscopy of frozen tissue sections was used to enhance the sensitivity of the analysis and to detect particles, scarce in most organs. Among the organs inspected in mice that received injections with control IgG/ASM nanocarriers, particles were found to accumulate only in liver and spleen (Fig. 3B), which may be due to uptake by resident phagocytes in these organs of the reticuloendothelial system (Muro et al., 2006a).

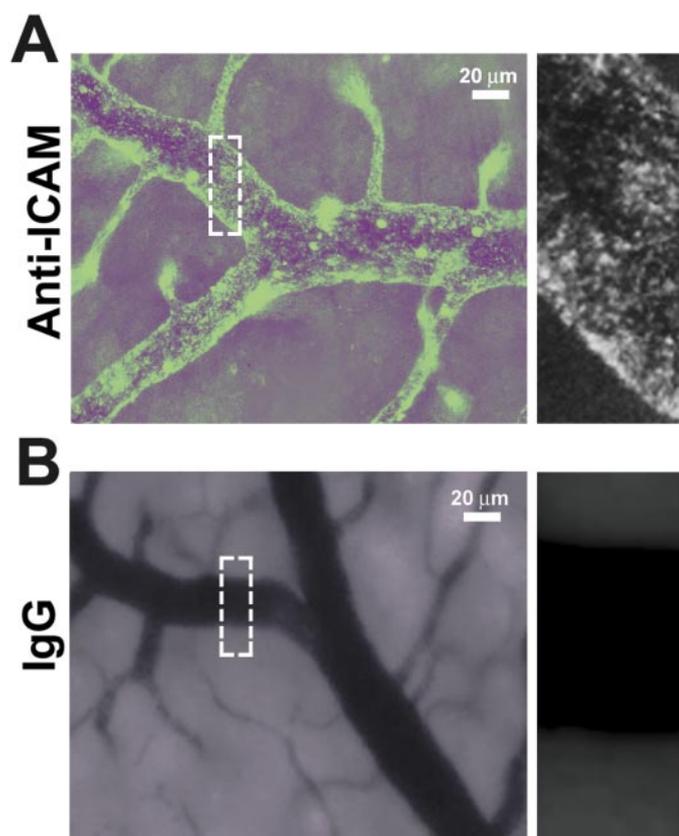To define the cellular localization of nanocarriers in the main

Fig. 2. Intravital microscopy of anti-ICAM/ASM particles bound to the mesentery microvasculature. Images show abundant and uniform binding of 180-nm anti-ICAM/ASM particles (A), but not control IgG/ASM particles (B), in a mesentery arteriole 30 min after injection. Scale bar, 20 μm. Right images are 5× magnifications of the vessel area marked by a dashed line box in the left image.

target organ, e.g., lung, we used red immunostaining to PE-CAM-1 (a pan-endothelial marker) and nuclear blue staining by 4,6-diamidino-2-phenylindole in frozen tissue sections of mouse lung isolated 30 min after injection of either anti-ICAM/ASM nanocarriers or control IgG/ASM counterparts. Results of this multilabeling analysis providing a high-resolution imaging of the tissue architecture (Fig. 4), revealed localization of anti-ICAM/ASM nanocarriers in pulmonary endothelial cells (note practically identical green and red labels), and showed a remarkably high, uniform, and specific uptake of anti-ICAM/ASM nanocarriers, but not IgG counterparts, through this organ, e.g., in the capillaries (right upper quadrant), vein (center), and artery (lower left quadrant).

Anti-ICAM/ASM Nanocarrier Accumulation Causes No Detectable Vascular Injury in Vivo. Binding of anti-ICAM nanocarriers to ICAM-1 expressed by cultured cells has been shown to induce immediate reorganization of the actin cytoskeleton into stress fibers, which ceased after ~2 to 3 h (Muro et al., 2003b). In theory, uncontrolled actin stress fiber formation, for example, in endothelial cells in the lung, may cause rapid cell contraction, disruption of vascular permeability, and edema (Etienne-Manneville et al., 2000; Stevens et al., 2000).

This scenario seems unlikely, because we did not observe any pathological signs in animals that received injections with the anti-ICAM/ASM nanocarriers used for the imaging experiments described above, nor signs of pathology or
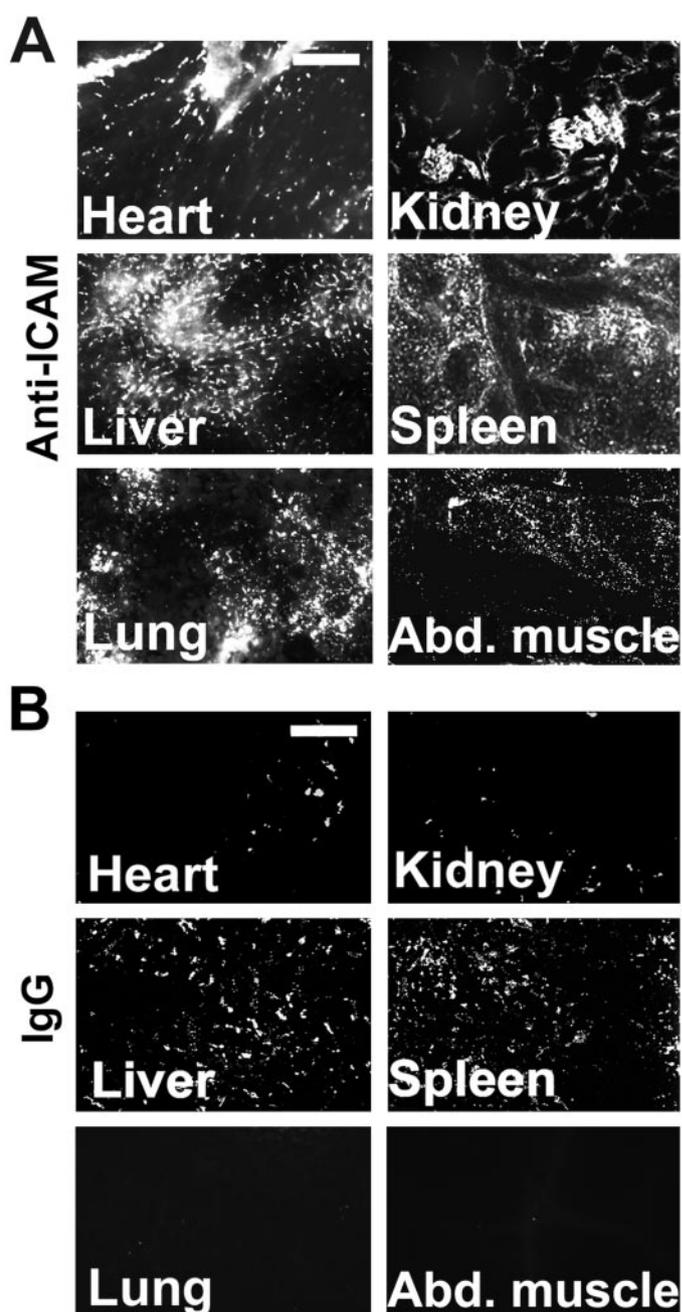

Fig. 3. Imaging anti-ICAM/ASM nanocarrier uptake in mouse organs. A, fluorescence images of whole (nonsectioned) organs isolated from C57BL/6 mice 30 min after injection of 180-nm green fluorescent anti-ICAM/ASM carriers. B, to maximize fluorescent detection, 10-μm-thick sections from frozen tissues were used in mice that received injections with control IgG/ASM counterparts. Scale bars, 100 μm.

edema in isolated mouse tissues. However, to more rigorously examine whether in vivo accumulation of anti-ICAM nanocarriers would elicit abnormal pulmonary permeability, we injected particles into mice and then we determined their potential effects in the lung (Fig. 5). First, we perfused, fixed, and isolated lung 30 min after injection, from which a lobe was cut open, permeabilized, and stained to detect actin filaments. A z-axis stack section of alveoli (Fig. 5A; Supplemental Movie 3) shows intact morphology, presence of actin cortical fibers (but not stress fibers) in the cell-cell border, and no evidence of a disrupted barrier or appearance of
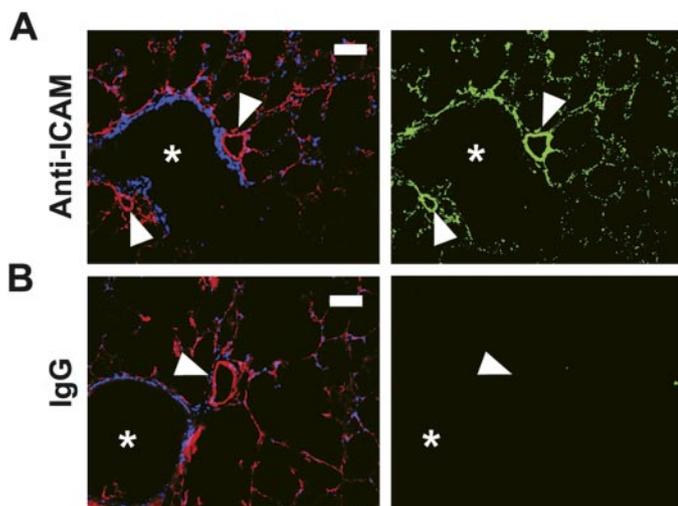
Fig. 4. Colocalization of anti-ICAM/ASM nanocarriers with endothelium in mouse lung. Ten-micrometer-thick frozen lung sections were stained with blue 4,6-diamidino-2-phenylindole to label cell nuclei and rat anti-mouse PECAM-1 followed by Texas Red-conjugated goat anti-rat, to label lung endothelium (left), and green fluorescent anti-ICAM/ASM nanocarriers (A) or control IgG/ASM counterparts (B) were imaged in the same sections (right). Small airways and vessels are indicated by asterisks and arrowheads, respectively. Scale bar, 100 μm.

blood cells in the alveolar lumen after nanocarrier injection, suggesting that anti-ICAM nanocarriers do not affect the integrity of the pulmonary permeability barrier. In accordance with this result, lung tissue in these animals seemed normal by histological examination of hematoxylin-and-eosin-stained tissue sections, and it did not show signs of disruption of the alveolar architecture, edema, or leukocyte infiltration in the alveoli (Fig. 5B).

To further confirm the safety of this approach, anti-ICAM nanocarriers were coinjected i.v. with ^{125}I-albumin, and transport of this tracer from the bloodstream to the lung tissue (which quantitatively characterizes edema) was determined as radioisotope lung-to-blood ratio 3 h after injection. Systemic injection of TNF-α, a proinflammatory cytokine known to disrupt vascular permeability, which was used as a positive control for lung edema in this study, caused a significant increase of albumin uptake in the lung, validating the sensitivity of this assay (Fig. 5B). In contrast, neither specific anti-ICAM nanocarriers nor control IgG nanocarriers elevated albumin uptake in the lung over control levels (Fig. 5B).

Biodistribution of Anti-ICAM/ASM Nanocarriers and Nontargeted Formulations. The imaging studies tracing model nanocarriers described above revealed rapid, effective, and safe in vivo targeting of anti-ICAM/ASM nanocarriers to mouse organs, particularly the lung, an important therapeutic target in type B NPD. To directly and quantitatively analyze the biodistribution of the enzyme cargo in vivo, we used formulations containing ^{125}I-ASM as a tracer. We compared the circulation time and organ accumulation of ^{125}I-ASM administered as either a nontargeted free enzyme or coupled to anti-ICAM biodegradable PLGA nanocarriers in anesthetized mice.

Anti-ICAM/^{125}I-ASM nanocarriers disappeared more rapidly from the circulation than free ^{125}I-ASM: 25.1 $\pm$ 9.6 versus 59.9 $\pm$ 6.5% ID remained in circulation at 1 min after injection, and 10.3 $\pm$ 1.0 versus 33.4 $\pm$ 4.2% ID at 15 min
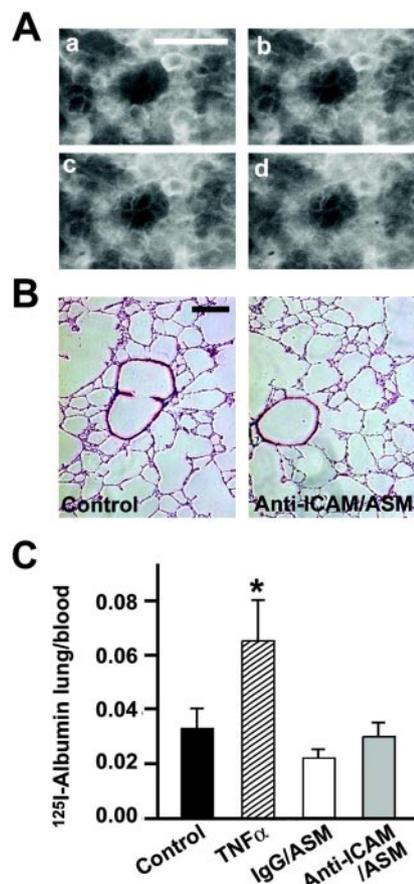

Fig. 5. Effects of anti-ICAM/ASM nanocarrier accumulation in lung tissue. A, staining of F-actin with Texas Red-phalloidin in permeabilized lung, 30 min after i.v. injection of C57BL/6 mice with 180-nm anti-ICAM/ASM nanocarriers. A z-section stack from the axial plane (a) to the base of an alveolus (d) was taken. Scale bar, 100 μm. See Supplemental Movie 3. B, hematoxylin and eosin staining of 10-μm-thick frozen sections from lung isolated 24 h after injection of either saline or anti-ICAM/ASM nanocarriers. Scale bar, 100 μm. C, level of ^{125}I-albumin coinjected with either saline (control), TNF-α, anti-ICAM/ASM, or IgG/ASM nanocarriers was determined in the lung and the blood 3 h after injection. Data are mean $\pm$ S.E.M. ($n \geq 3$ mice). *, $p < 0.05$ (Student's t test).

after injection, respectively (Fig. 6A, inset). Such an accelerated blood clearance probably reflects endothelial binding and accumulation of anti-ICAM/ASM nanocarriers in vascularized organs, as shown by prior imaging results. Consistent with this notion, anti-ICAM/^{125}I-ASM nanocarriers effectively accumulated in mouse organs, determined at 30 min after injection (Fig. 6A), including kidney, heart, liver, spleen, and primarily lung (e.g., 50.7 $\pm$ 5.6% ID per gram of lung for anti-ICAM/^{125}I-ASM nanocarriers versus 6.5 $\pm$ 0.6% ID per gram of lung for free ^{125}I-ASM). Normalization per gram of tissue permitted comparisons of the uptake level in organs of different size. On the absolute scale, spleen, liver, and lung, the main target organs in type B NPD, received the highest delivery of enzyme by anti-ICAM/^{125}I-ASM nanocarriers (3.5 $\pm$ 0.7, 39.6 $\pm$ 1.4, and 8.1 $\pm$ 1.0% of the total ID versus 0.8 $\pm$ 0.06, 22.9 $\pm$ 2.6, and 0.9 $\pm$ 0.1% ID, respectively, for free ^{125}I-ASM; Fig. 6B). The organ-to-blood localization ratio was significantly higher for anti-ICAM/^{125}I-ASM nanocarriers versus ^{125}I-ASM, particularly in the lung (e.g., 7.7 $\pm$ 1.2 versus 0.3 $\pm$ 0.03 for free ^{125}I-ASM; Fig. 6C), reflecting the high tissue specificity of ICAM-1-targeted enzyme formulations.
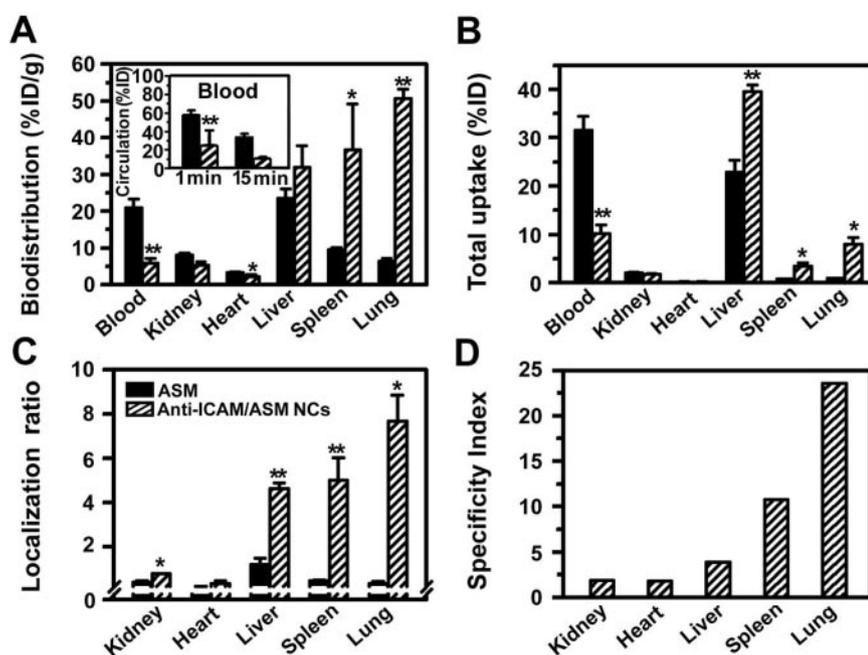
Fig. 6. Pharmacokinetics of anti-ICAM/ASM nanocarriers. Biodistribution of ^{125}I-labeled ASM injected i.v. as either a free enzyme (black bars) or coupled to 270-nm anti-ICAM biodegradable PLGA nanocarriers (hatched bars), 30 min after injection. Data were calculated as %ID/g of organ (A), to permit relative comparisons between organs with different weight; %ID per organ (B), to estimate the total accumulation; localization ratio (%ID/g in an organ:%ID/g in blood) (C), to correct to differences in the blood level of the formulations; and the specificity index (calculated as the localization ratio of targeted to nontargeted formulations) (D), which reflects the specificity of ICAM-1 targeting. The inset in A shows nanocarrier clearance from blood, calculated as %ID. Data are mean ± S.E.M. ($n \geq 5$ mice). Statistical differences between the noncoupled enzyme and anti-ICAM PLGA carriers are depicted by asterisks. *, $p < 0.05$ and **, $p < 0.01$ (Student's t test).

Anti-ICAM/ASM nanocarriers showed higher uptake in all organs versus nontargeted free ASM: the -fold increase or specificity index achieved was 1.8 in heart, 1.9 in kidney, 3.9 in liver, 10.8 in spleen, and 23.6 in lung (Fig. 6D). Such an enhanced delivery to lung in particular was not due to nonspecific particle uptake or mechanical retention. Control IgG/^{125}I-ASM nanocarriers accumulated in liver and spleen (Table 1), confirming imaging results showing retention of these particles in the reticuloendothelial system (Fig. 3B). However, in accord with imaging data shown in Fig. 4, IgG/^{125}I-ASM nanocarriers did not accumulate in lung (Table 1). As a result, the lung-specific delivery index of anti-ICAM/ASM over IgG/ASM nanocarriers was 21.3 (Table 1).

High levels of pulmonary and hepatic uptake of anti-ICAM/ASM nanocarriers agreed with high levels of ICAM-1 expression in these organs (Table 2); yet, in other organs uptake of anti-ICAM/ASM nanocarriers did not show a good correlation with the relative levels of ICAM-1 expression (Table 2).

ASM Delivery via ICAM-1 Targeting in a Niemann-Pick Disease Mouse Model. Finally, we aimed at obtaining evidence for enzyme delivery by ICAM-1 targeting in vivo in a pathologically relevant context, the ASMKO model of types A and B NPD (He et al., 1999; Miranda et al., 2000; Dhami et al., 2001). ASMKO mice showed elevated ICAM-1 expression in lung (2.7 ± 0.6-fold over C57BL/6 mice; Table 2), which correlates with pulmonary inflammation typical in these animals (Marathe et al., 1998).

We traced radiolabeled recombinant ASM injected i.v. in ASMKO mice as either free ^{125}I-ASM or ^{125}I-ASM coupled to reporter anti-ICAM nanocarriers, and blood and/or organ samples were collected at 1, 15, and 30 min after injection to determine the radioisotope content (Fig. 7). As found in wild-type mice, anti-ICAM/^{125}I-ASM nanocarriers rapidly disappeared from the circulation (9.9 ± 2.7 and 0.5 ± 0.1% ID at 1 and 15 min after injection; Fig. 7A, inset) and they accumulated in organs, including kidney, heart, liver, spleen, and lung (4.3 ± 0.2, 2.7 ± 0.6, 16.3 ± 3.6, 16.0 ± 2.4, and 98.9 ±

20.8% ID/g; Fig. 7A), as determined at 30 min after injection. Spleen, liver, and lung, main targets for type B NPD, received the highest enzyme delivery: 1.7 ± 0.5, 25.1 ± 3.8, and 20.0 ± 4.2% of the injected dose (Fig. 7B). In addition, in these animals, organ-to-blood localization ratio of anti-ICAM/^{125}I-ASM nanocarriers was higher than that of the free enzyme, as observed in the previous experimental series in wild-type animals (the localization ratio for anti-ICAM/^{125}I-ASM was 2.9 ± 0.4 in kidney, 1.4 ± 0.3 in heart, 12.4 ± 4.6 in liver, 10.5 ± 1.5 in spleen, and 59.9 ± 4.2 in lung; Fig. 7C).

In contrast, naked ^{125}I-ASM circulated for longer periods (62.2 ± 4.3 and 58.7 ± 19.5% ID at 1 and 15 min after injection; Fig. 7A), and it resulted in lower organ-to-blood uptake (the localization ratio was 0.3 ± 0.05 in kidney, 0.2 ± 0.03 in heart, 0.9 ± 0.2 in liver, 0.5 ± 0.07 in spleen, and 0.3 ± 0.03 in lung; Fig. 7C). Hence, coupling ASM to anti-ICAM nanocarriers markedly enhanced the specific delivery of circulating ASM to all organs analyzed over that of the nontargeted enzyme (the specificity index was 9.9 in kidney, 7.3 in heart, 12.5 in liver, 21.2 in spleen, and 216.2 in lung; Fig. 7D), reflecting the high targeting potential of anti-ICAM/^{125}I-ASM nanocarriers in this disease model.

Discussion

ERT is one of the most viable treatments for type B NPD, as well as other lysosomal storage disorders (Desnick and Schuchman, 2002). However, suboptimal delivery of recombinant lysosomal enzymes to certain target organs (Figs. 6 and 7) reduces the efficacy of this strategy. Targeting ERTs to specific cell surface determinants (e.g., using chimeric enzymes containing targeting moieties; Xia et al., 2001; LeBowitz et al., 2004; Prince et al., 2004; Zhang et al., 2007) may facilitate delivery to the desired pathological sites.

In this context, nanoscale size carriers represent highly promising vehicles for ERT because they can be modified (e.g., with antibodies) to provide specific targeting, control of

TABLE 1
Biodistribution of anti-ICAM/ASM vs. IgG/ASM nanocarriers in mice
Blood and organ levels of 180-nm-diameter polystyrene particles carrying ^{125}I-ASM and either anti-ICAM or control IgG 30 min after i.v. injection in anesthetized C57Bl/6 mice. Data are mean ± S.E.M. ($n \geq 6$ mice).

	Blood		Kidney		Heart		Liver		Spleen		Lung	
	Anti-ICAM	IgG	Anti-ICAM	IgG	Anti-ICAM	IgG	Anti-ICAM	IgG	Anti-ICAM	IgG	Anti-ICAM	IgG
%ID	4.1 ± 0.4	3.4 ± 0.3	1.4 ± 0.05*	0.9 ± 0.1	0.4 ± 0.03	0.3 ± 0.04	39.0 ± 2.8***	58.9 ± 1.9	4.0 ± 0.4	4.6 ± 0.9	22.8 ± 3.0***	0.9 ± 0.2
%ID/g	2.6 ± 0.3	2.0 ± 0.1	4.7 ± 0.2**	3.2 ± 0.5	3.7 ± 0.3	3.1 ± 0.2	36.4 ± 2.8**	53.9 ± 2.6	47.3 ± 5.1	58.2 ± 14.2	140.8 ± 17.0***	6.9 ± 1.5
LR			2.0 ± 0.2	1.3 ± 0.4	1.6 ± 0.2	1.1 ± 0.2	16.6 ± 2.5	20.0 ± 4.6	22.3 ± 3.8	20.7 ± 7.8	61.5 ± 11.3***	2.9 ± 1.1
Specificity index			1.5		1.5		0.8		1.1		21.3	

* $p < 0.05$, ** $p < 0.01$, and *** $p < 0.001$ (Student's t test).

the circulation time, and modulate tissue accumulation of the carried drugs (Langer, 1998; Moghimi and Szebeni, 2003; Panyam and Labhasetwar, 2003; Muro and Muzykantov, 2005). ERT with enzymes that are deficient in genetic disorders, particularly those that affect peripheral organs, such as the lysosomal storage disorder type B NPD, also represents a promising, yet unexplored, application of these nanomedicine technologies. As "proof-of-principle" for this approach, our previous study showed that anti-ICAM nanocarriers carrying recombinant ASM efficiently reached lysosomes in ICAM-1-expressing cells (endothelial cells and NPD patient fibroblasts), and they attenuated intracellular sphingomyelin excess storage (Muro et al., 2006b).

This work additionally demonstrates enhanced delivery of recombinant ASM in naive and ASMKO mice by anti-ICAM polymer nanocarriers, validating ERT targeting assisted by polymer particles in vivo. Fluorescent real-time imaging showed fast and profuse binding to the vascular endothelium of anti-ICAM/ASM particles injected systemically, even in the case of arterioles (Figs. 1A and 2A) where relatively high shear stress may reduce collisions of particles with the vascular wall and/or drag bound particles off the target (Sakhalkar et al., 2003; Ali et al., 2004). This effective targeting is probably due to high affinity of multivalent anti-ICAM/ASM particles. In a previous study, we showed that 100- to 200-nm polymer nanocarriers coated with >200 copies of ICAM-1 antibody displayed ~100-fold enhanced affinity compared with the naked antibody and that they efficiently targeted vascularized organs (Muro et al., 2006a).

Liver and lung showed higher expression of ICAM-1 (Table 2) and absolute accumulation of anti-ICAM/ASM nanocarriers (Figs. 6 and 7). Yet, ICAM-1 is not only expressed by endothelial cells but also other cells in the tissues, which may explain why targeting of anti-ICAM/ASM nanocarriers to other organs did not entirely correlate with ICAM-1 expression in organ homogenates. Differences in the ratio of the vasculature to the entire organ mass may also influence the relative accumulation of anti-ICAM/ASM nanocarriers, such as the case of their profuse targeting to the lung.

Coupling ASM to the surface of anti-ICAM nanocarriers did not compromise targeting efficiency (e.g., 185 ± 24% ID/g of lung for cargo-free reporter anti-ICAM polystyrene nanocarriers prepared at antibody surface saturation (Muro et al., 2006a) versus 141 ± 17% ID/g of lung for anti-ICAM/ASM counterparts), despite implying a decrease in the antibody surface density. Perhaps, inherent affinity of glycosylated ASM to mannose and/or mannose-6-phosphate receptors (He et al., 1999; Dhami and Schuchman, 2004), enhanced by particle multivalency, may have contributed to this result.

In addition, ASM was coupled to anti-ICAM polymer nanocarriers by protein surface absorption, avoiding chemical modification that may be detrimental to its structure and/or activity. This was possible for ASM because it will only become activated at acidic pH within lysosomal compartments (Neufeld, 1980; He et al., 1999); hence, the injected enzyme can be considered a prodrug, not requiring encapsulation. The resulting formulations were relatively stable upon injection in the circulation. Low affinity of naked ASM results in longer circulation times (~35% ID in circulation 30 min after injection; Figs. 6 and 7). Because most of the enzyme administered as an anti-ICAM nanocarrier formulation was recovered in the tissue and not in the circulating fraction (~5%

TABLE 2
ICAM-1 expression in mouse organs

Western Blot and densitometry analysis of ICAM-1 (ICAM-1-to-actin ratio) from whole organ homogenates [either control (Ctr) C57Bl/6 or ASMKO (KO) mice]. Data represent mean ± S.E.M. ($n \geq 4$ samples from two animals).

	Kidney (Ctr)	Heart (Ctr)	Liver (Ctr)	Spleen (Ctr)	Lung (Ctr)	Lung (KO)
ICAM-1/actin	0.6 ± 0.2	0.5 ± 0.2	1.8 ± 0.2	0.3 ± 0.02	1.4 ± 0.3	3.7 ± 0.9
Normalized to lung (Ctr; %)	47.1 ± 12.5	39.1 ± 12.9	127.8 ± 14.1	20.4 ± 1.5	100 ± 23.6	266.2 ± 0.7*

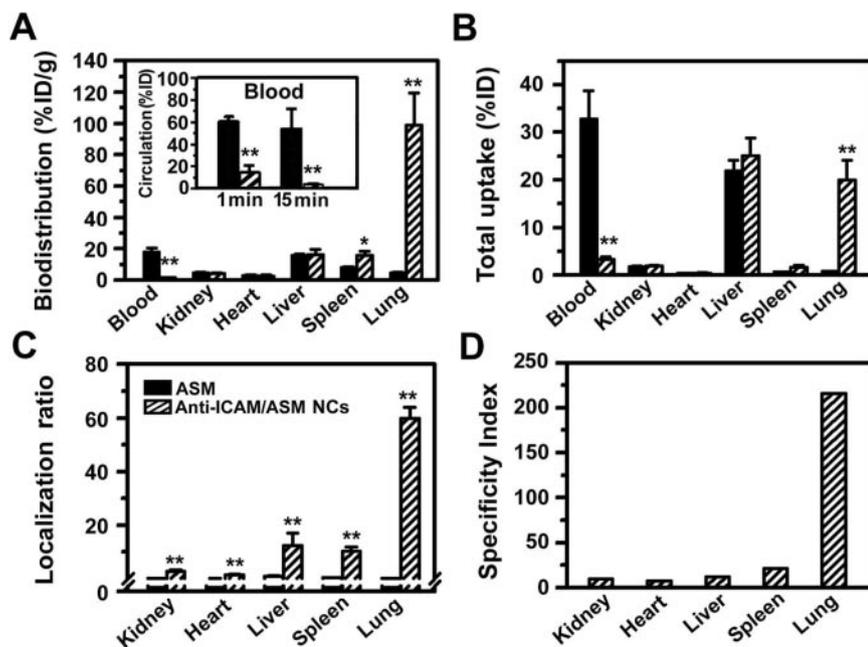* $p < 0.05$ (Student's t test).

Fig. 7. ASM delivery by anti-ICAM/ASM nanocarriers in Niemann-Pick disease mouse model. Biodistribution of ^{125}I-labeled ASM 30 min after i.v. injection in anesthetized ASM knockout mice, calculated as %ID per gram (A), %ID per organ (B), localization ratio (C), and specificity index (D). A comparison of naked ^{125}I-ASM (black bars) and 180-nm reporter anti-ICAM/^{125}I-ASM polystyrene nanocarriers (hatched bars) is shown. The inset in A shows nanocarrier clearance from blood (%ID). Data are mean ± S.E.M. ($n \geq 5$ mice). Statistical differences between free enzyme and anti-ICAM nanocarriers are depicted by asterisks. *, $p < 0.05$ and **, $p < 0.01$ (Student's t test).

total recovered enzyme in circulation versus ~70% in tissues), this indicates that the enzyme remained to linked anti-ICAM nanocarriers upon i.v. injection.

Enzyme loading by surface absorption and endothelial targeting of the resulting nanocarriers was effective both for fluorescent polystyrene nanocarriers (used in this work as a model) and nanocarriers formulated from biocompatible Food and Drug Administration-approved PLGA, a safe polymer that can be metabolized in tissues and displays low toxic and immunogenic effects (Matsusue et al., 1995; Cleland, 1997; Jain et al., 2000; Avgoustakis et al., 2002; Moghimi and Szebeni, 2003; Panyam and Labhasetwar, 2003). Thus, it represents a highly promising formulation for future translational studies on ERT delivery.

As in wild-type mice (Fig. 6), enhanced ASM delivery to type B NPD target organs was markedly effective in ASMKO mice (Fig. 7). This is a crucial finding because NPD inflammatory pathology in this animal model (as in type B NPD patients) may have blocked ICAM-1 by adherent leukocytes (Springer, 1994), decreasing its accessibility. In contrast, a highly efficient pulmonary uptake of anti-ICAM/ASM nanocarriers was observed in ASMKO mice (Fig. 7), which correlated with elevated pulmonary ICAM-1 expression over control mice (Table 2), probably due to increased levels of inflammatory factors in NPD pathology (Springer, 1994; Muro, 2007).

To our knowledge, this is the first work exploring lysosomal enzyme delivery assisted by targeted polymer nanocarriers in vivo. As shown, ICAM-1 targeting provided a means to enhance delivery of recombinant ASM to vascular endothelium both in control mice and the mouse model for type B NPD (Figs. 1, 6, and 7). Of particular importance, anti-ICAM particle formulations achieved significantly improved pulmonary uptake compared with that of the naked enzyme, providing a means to enhance enzyme delivery to this critical type B NPD target organ. It is apparent, therefore, that this strategy holds considerable promise as an alternative, more efficient delivery modality for ERT.

References

Ali M, Hicks AE, Hellewell PG, Thoma G, and Norman KE (2004) Polymers bearing sLex-mimetics are superior inhibitors of E-selectin-dependent leukocyte rolling in vivo. *FASEB J* **18:**152–154.

Avgoustakis K, Beletsi A, Panagi Z, Klepetsanis P, Karydas AG, and Ithakissios DS (2002) PLGA-mPEG nanoparticles of cisplatin: in vitro nanoparticle degradation, in vitro drug release and in vivo drug residence in blood properties. *J Control Release* **79:**123–135.

Bloemen PG, Henricks PA, van Bloois L, van den Tweel MC, Bloem AC, Nijkamp FP, Crommelin DJ, and Storm G (1995) Adhesion molecules: a new target for immunoliposome-mediated drug delivery. *FEBS Lett* **357:**140–144.

Cleland JL (1997) Protein delivery from biodegradable microspheres. *Pharm Biotechnol* **10:**1–43.

DeGraba T, Azhar S, Dignat-George F, Brown E, Boutiere B, Altarescu G, McCarron R, and Schiffmann R (2000) Profile of endothelial and leukocyte activation in Fabry patients. *Ann Neurol* **47:**229–233.

Desnick RJ and Schuchman EH (2002) Enzyme replacement and enhancement therapies: lessons from lysosomal disorders. *Nat Rev Genet* **3:**954–966.

Dhami R and Schuchman EH (2004) Mannose 6-phosphate receptor-mediated uptake is defective in acid sphingomyelinase-deficient macrophages: implications for Niemann-Pick disease enzyme replacement therapy. *J Biol Chem* **279:**1526–1532.

Dhami R, He X, Gordon RE, and Schuchman EH (2001) Analysis of the lung pathology and alveolar macrophage function in the acid sphingomyelinase-deficient mouse model of Niemann-Pick disease. *Lab Invest* **81:**987–999.

Du H, Levine M, Ganesa C, Witte DP, Cole ES, and Grabowski GA (2005) The role of mannosylated enzyme and the mannose receptor in enzyme replacement therapy. *Am J Hum Genet* **77:**1061–1074.

Dziubla TD, Karim A, and Muzykantov VR (2005) Polymer nanocarriers protecting active enzyme cargo against proteolysis. *J Control Release* **102:**427–439.

Etienne-Manneville S, Manneville JB, Adamson P, Wilbourn B, Greenwood J, and Couraud PO (2000) ICAM-1-coupled cytoskeletal rearrangements and transendothelial lymphocyte migration involve intracellular calcium signaling in brain endothelial cell lines. *J Immunol* **165:**3375–3383.

Futerman AH and van Meer G (2004) The cell biology of lysosomal storage disorders. *Nat Rev Mol Cell Biol* **5:**554–565.

He X, Miranda SR, Xiong X, Dagan A, Gatt S, and Schuchman EH (1999) Characterization of human acid sphingomyelinase purified from the media of overexpressing Chinese hamster ovary cells. *Biochim Biophys Acta* **1432:**251–264.

Institute of Laboratory Animal Resources (1996) *Guide for the Care and Use of Laboratory Animals* 7th ed. Institute of Laboratory Animal Resources, Commission on Life Sciences, National Research Council, Washington DC.

Jain RA, Rhodes CT, Railkar AM, Malick AW, and Shah NH (2000) Controlled delivery of drugs from a novel injectable in situ formed biodegradable PLGA microsphere system. *J Microencapsul* **17:**343–362.

Langer R (1998) Drug delivery and targeting. *Nature* **392:**5–10.

LeBowitz JH, Grubb JH, Maga JA, Schmiel DH, Vogler C, and Sly WS (2004) Glycosylation-independent targeting enhances enzyme delivery to lysosomes and decreases storage in mucopolysaccharidosis type VII mice. *Proc Natl Acad Sci U S A* **101:**3083–3088.

Marathe S, Schissel SL, Yellin MJ, Beatini N, Mintzer R, Williams KJ, and Tabas I (1998) Human vascular endothelial cells are a rich and regulatable source of secretory sphingomyelinase. Implications for early atherogenesis and ceramide-mediated cell signaling. *J Biol Chem* **273:**4081–4088.

Marlin SD and Springer TA (1987) Purified intercellular adhesion molecule-1 (ICAM-1) is a ligand for lymphocyte function-associated antigen 1 (LFA-1). *Cell* **51:**813–819.

Matsusue Y, Hanafusa S, Yamamuro T, Shikinami Y, and Ikada Y (1995) Tissue reaction of bioabsorbable ultra high strength poly (L-lactide) rod. A long-term study in rabbits. *Clin Orthop Relat Res* **317:**246–253.

Miranda SR, He X, Simonaro CM, Gatt S, Dagan A, Desnick RJ, and Schuchman EH (2000) Infusion of recombinant human acid sphingomyelinase into Niemann-Pick disease mice leads to visceral, but not neurological, correction of the pathophysiology. *FASEB J* **14:**1988–1995.

Moghimi SM and Szebeni J (2003) Stealth liposomes and long circulating nanoparticles: critical issues in pharmacokinetics, opsonization and protein-binding properties. *Prog Lipid Res* **42:**463–478.

Murciano JC, Muro S, Koniaris L, Christofidou-Solomidou M, Harshaw DW, Albelda SM, Granger DN, Cines DB, and Muzykantov VR (2003) ICAM-directed vascular immunotargeting of antithrombotic agents to the endothelial luminal surface. *Blood* **101:**3977–3984.

Muro S (2007) ICAM-1 and VCAM-1, in *Endothelial Biomedicine* (Aird WC ed) pp 1058–1070, Cambridge University Press, Cambridge, UK.

Muro S, Cui X, Gajewski C, Murciano JC, Muzykantov VR, and Koval M (2003a) Slow intracellular trafficking of catalase nanoparticles targeted to ICAM-1 protects endothelial cells from oxidative stress. *Am J Physiol Cell Physiol* **285:**C1339–C1347.

Muro S, Dziubla T, Qiu W, Leferovich J, Cui X, Berk E, and Muzykantov VR (2006a) Endothelial targeting of high-affinity multivalent polymer nanocarriers directed to intercellular adhesion molecule 1. *J Pharmacol Exp Ther* **317:**1161–1169.

Muro S and Muzykantov VR (2005) Targeting of antioxidant and anti-thrombotic drugs to endothelial cell adhesion molecules. *Curr Pharm Des* **11:**2383–2401.

Muro S, Schuchman EH, and Muzykantov VR (2006b) Lysosomal enzyme delivery by ICAM-1-targeted nanocarriers bypassing glycosylation- and clathrin-dependent endocytosis. *Mol Ther* **13:**135–141.

Muro S, Wiewrodt R, Thomas A, Koniaris L, Albelda SM, Muzykantov VR, and Koval M (2003b) A novel endocytic pathway induced by clustering endothelial ICAM-1 or PECAM-1. *J Cell Sci* **116:**1599–1609.

Neufeld EF (1980) The uptake of enzymes into lysosomes: an overview. *Birth Defects Orig Artic Ser* **16:**77–84.

Panyam J and Labhasetwar V (2003) Biodegradable nanoparticles for drug and gene delivery to cells and tissue. *Adv Drug Deliv Rev* **55:**329–347.

Prince WS, McCormick LM, Wendt DJ, Fitzpatrick PA, Schwartz KL, Aguilera AI, Koppaka V, Christianson TM, Vellard MC, Pavloff N, et al. (2004) Lipoprotein receptor binding, cellular uptake, and lysosomal delivery of fusions between the receptor-associated protein (RAP) and α-L-iduronidase or acid α-glucosidase. *J Biol Chem* **279:**35037–35046.

Rejman J, Oberle V, Zuhorn IS, and Hoekstra D (2004) Size-dependent internalization of particles via the pathways of clathrin- and caveolae-mediated endocytosis. *Biochem J* **377:**159–169.

Sakhalkar HS, Dalal MK, Salem AK, Ansari R, Fu J, Kiani MF, Kurjiaka DT, Hanes J, Shakesheff KM, and Goetz DJ (2003) Leukocyte-inspired biodegradable particles that selectively and avidly adhere to inflamed endothelium in vitro and in vivo. *Proc Natl Acad Sci U S A* **100:**15895–15900.

Schuchman EH, Desnick R.J (2000) Niemann-Pick disease types A and B: acid sphingomyelinase deficiencies, in *Lysosomal Disorders. The Metabolic and Molecular Bases of Inherited Disease*, 8th ed (Scriver C, Beaudet A, Sly W, Valle D, Childs B, Kinzler K, and Vogelstein B eds), McGraw-Hill Companies, New York.

Springer TA (1994) Traffic signals for lymphocyte recirculation and leukocyte emigration: the multistep paradigm. *Cell* **76:**301–314.

Stevens T, Garcia JG, Shasby DM, Bhattacharya J, and Malik AB (2000) Mechanisms regulating endothelial cell barrier function. *Am J Physiol Lung Cell Mol Physiol* **279:**L419–L422.

Villanueva FS, Jankowski RJ, Klibanov S, Pina ML, Alber SM, Watkins SC, Brandenburger GH, and Wagner WR (1998) Microbubbles targeted to intercellular adhesion molecule-1 bind to activated coronary artery endothelial cells. *Circulation* **98:**1–5.

Weiner RE, Sasso DE, Gionfriddo MA, Thrall RS, Syrbu S, Smilowitz HM, and Vento J (2001) Early detection of oleic acid-induced lung injury in rats using (111)In-labeled anti-rat intercellular adhesion molecule-1. *J Nucl Med* **42:**1109–1115.

Xia H, Mao Q, and Davidson BL (2001) The HIV Tat protein transduction domain improves the biodistribution of beta-glucuronidase expressed from recombinant viral vectors. *Nat Biotechnol* **19:**640–644.

Zhang Y, Wang Y, Boado RJ, and Pardridge WM (2008) Lysosomal enzyme replacement of the brain with intravenous non-viral gene transfer. *Pharmacol Res* **25:**400–406.

Address correspondence to: Dr. Silvia Muro, Department of Pharmacology, John Morgan Bldg., 3620 Hamilton Walk, Philadelphia, PA 19104-6068. E-mail: silvia@mail.med.upenn.edu